# Hardware Design and Fault-Tolerant Synthesis for Digital Acoustofluidic Biochips

Zhanwei Zhong , Haodong Zhu, Peiran Zhang, James Morizio, *Member, IEEE*, Tony Jun Huang, *Fellow, IEEE*, and Krishnendu Chakrabarty , *Fellow, IEEE* 

Abstract—A digital microfluidic biochip (DMB) is an attractive platform for automating laboratory procedures in microbiology. To overcome the problem of cross-contamination due to fouling of the electrode surface in traditional DMBs, a contactless liquid-handling biochip technology, referred to as acoustofluidics, has recently been proposed. A major challenge in operating this platform is the need for a control signal of frequency 24 MHz and voltage range  $\pm 10/\pm 20~{\rm V}$  to activate the IDT units in the biochip. In this paper, we present a hardware design that can efficiently activate/de-activated each IDT, and can fully automate an bio-protocol. We also present a fault-tolerant synthesis technique that allows us to automatically map biomolecular protocols to acoustofluidic biochips. We develop and experimentally validate a velocity model, and use it to guide co-optimization for operation scheduling, module placement, and droplet routing in the presence of IDT faults. Simulation results demonstrate the effectiveness of the proposed synthesis method. Our results are expected to open new research directions on design automation of digital acoustofluidic biochips.

Index Terms—Biochip, digital acoustofluidics, fault-tolerence, hardware design.

#### I. INTRODUCTION

ICROFLUIDIC biochips are now being increasingly used for high-throughput DNA sequencing, point-of-care clinical diagnostics, and immunoassays [1], [2]. In particular, digital microfluidic biochips (DMBs) are especially promising [3]. They manipulate liquid as discrete droplets of sub-nano volumes based on the principle of electrowetting-on-dielectric

Manuscript received March 28, 2020; revised May 18, 2020 and July 11, 2020; accepted August 17, 2020. Date of publication August 20, 2020; date of current version October 15, 2020. This work was supported in part by the U.S. National Science Foundation under Grant CCF-1702596, in part by the National Institutes of Health under Grant R01GM132603, Grant R01GM135486, Grant UG3TR002978, Grant R33CA223908, Grant R01GM127714, and Grant R01HD086325, and in part by the US Army Medical Research Acquisition Activity under Grant W81XWH-18-1-0242. Conflict of Interest: T.J.H. has co-founded a start-up company, Ascent Bio-Nano Technologies Inc., to commercialize technologies involving acoustofluidics and acoustic tweezers. A preliminary version of this paper was published in BioCAS, 2019. This paper was recommended by Associate Editor Prof. Maide Bucolo. (Corresponding author: Zhanwei Zhong.)

Zhanwei Zhong, James Morizio, and Krishnendu Chakrabarty are with the Department of Electrical and Computer Engineering, Duke University, Durham, NC 27705 USA (e-mail: zzwzhong698800@gmail.com; jmorizio@ee.duke.edu; krish@ee.duke.edu).

Haodong Zhu, Peiran Zhang, and Tony Jun Huang are with the Department of Mechanical Engineering and Materials Science, Duke University, Durham, NC 27705 USA (e-mail: haodong.zhu@duke.edu; zhangpeiran.1992@gmail.com; tony.huang@duke.edu).

Color versions of one or more of the figures in this article are available online at https://ieeexplore.ieee.org.

Digital Object Identifier 10.1109/TBCAS.2020.3018136

under voltage-based electrode actuation [1]. DMBs have been commercially adopted for sample preparation [4], infectious disease testing [5] and neonatal screening [6]. In addition, microelectrode-dot-array (MEDA) biochips have been demonstrated with integrated sensors and real-time feedback [7]–[10]. A particular advantage of MEDA is that it allows the manipulation of droplets of various sizes.

Despite these advances, today's DMB platforms suffer from a fundamental limitation. They all rely on physical contact between the carrier droplet and an electrode in order to hold, transport or manipulate droplets. Therefore, traces of a droplet inevitably adsorb on to the contact surface and the residue can subsequently contaminate another droplet [11]. This problem is especially severe for larger molecules such as proteins. While such cross-contamination can be reduced using a layer of inert liquid, e.g., silicone oil, it cannot be eliminated completely [12]. Thus, the risk of cross-contamination due to undesirable fouling of the electrode surface inherently limits the transportation and repetitive actuation of droplets with sticky biomolecules such as those in whole and undiluted blood.

To overcome the above limitation, a contactless droplethandling platform, namely *digital acoustofluidic biochips*, has been proposed [13]. On this platform, droplets float on an inert, immiscible layer of oil that effectively isolates a droplet from the solid surface. An array of interdigital transducers (IDTs) constitutes the actuators of this platform. By turning on/off these IDTs, we can achieve droplet operations such as holding, transportation, splitting, and mixing on this platform.

As shown in Fig. 1(a), in order to manipulate droplets along the horizontal plane without any direct contact with the surface, a denser carrier layer of fluorinated oil is added on top of the substrate. The fluorinated oil is not only used as an isolation layer upon which the droplets float, but also as an actuator to drive droplets via the drag force induced by acoustic streaming. When an immersed IDT is activated, it generates bulk waves in the oil layer and surface acoustic waves (SAWs) in the substrate layer. As a result of both bulk waves and SAWs, two symmetric fluid jets emerge out of the substrate plane and they induce two localized symmetric hydrodynamic traps near the flanks of the transducer. An IDT acts as a "micropump" that pumps fluid out along the y-axis and pumps fluid in along the x-axis.

Fig. 1(b) shows the cross-sectional view of streamlines in the x-z plane. Specifically, a floating droplet near the side of an activated IDT will be automatically translated in the x-axis direction toward the IDT following a hydrodynamic gradient.

1932-4545 © 2020 IEEE. Personal use is permitted, but republication/redistribution requires IEEE permission. See https://www.ieee.org/publications/rights/index.html for more information.

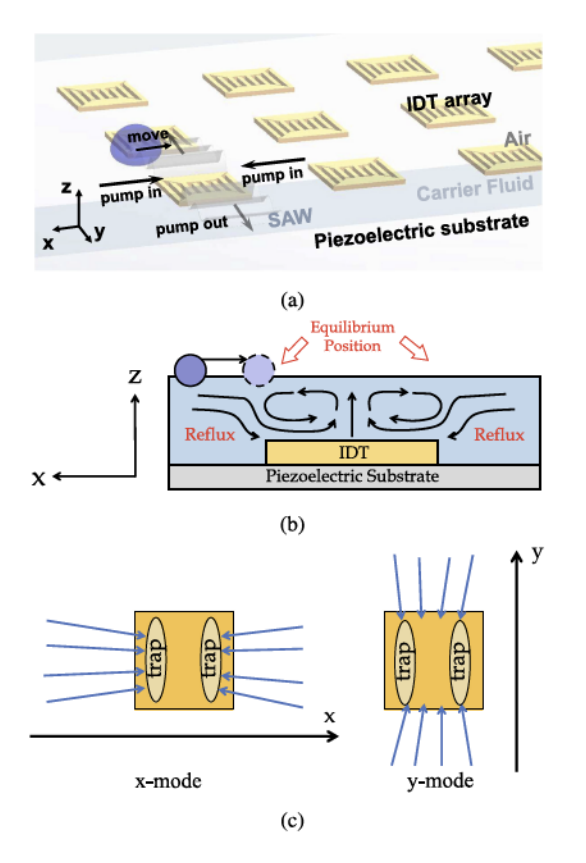


Fig. 1. (a) Working principle of IDTs; (b) fluidic flow viewed in the x-z plane; (c) two working modes for an IDT.

Eventually, the droplet is stabilized at one of the hydrodynamic equilibrium positions, due to the force balance between the reflux from the far field and the counter-rotating vortex near the flanks of the IDT. During the droplet-trapping process, the far field reflux first pulls the droplet toward the transducer. Then the counter-rotating vortex resists the reflux, and finally pinches the droplet. The equilibrium positions are referred to as "traps".

A preliminary system-level design of an acoustofluidics platform is described in Section II. This design suffers from a number of drawbacks that must be alleviated before this technology can be advanced further.

In addition to the system-level design problems, a key step in utilizing DMBs for microbiology is the control software that maps biomolecular protocols to the chip. There has been a considerable amount of work on high-level synthesis for DMBs [14]–[19]. Even though acoustofluidic biochips utilize a completely different actuation mechanism to manipulate droplets, they can also benefit from advances in design automation that map bioprotocol synthesis to the IDT array. In particular, synthesis methods developed earlier for MEDA [14] can potentially be adapted for acoustofluidics because both these platforms can handle droplets of various sizes.

Since device-level design has received considerable attention in recent years [13], [20], this paper focuses on the system-level integration and control-software design. The main contributions of this paper are as follows:

 A hardware design, referred to as an IDT-driver unit, is proposed to generate the 24 MHz sinusoidal signal with 20/40

- Vpp, which obviates the need for a function generator as well as the bulky microwave amplifier.
- A PCB-board design that integrates 16 IDT-driver units is fabricated and validated in the laboratory. This PCB-board design is able to control a biochip with 16 IDTs (i.e., 4 × 4 IDT array).
- A mathematical model is developed to characterize droplet velocity in acoustofluidics. This model is needed to make informed decisions at various steps during bio-protocol synthesis. The velocity model is validated using experimental results on fabricated chips.
- Solutions for operation scheduling, module placement and droplet routing are presented. In particular, fault tolerance is integrated in droplet routing, and an A\*-based routing algorithm is presented to minimize routing time in the presence of faulty IDTs.

The remainder of the paper is organized as follows. Section II presents a preliminary system-level design of an acoustofluidics platform and its drawbacks. Section III presents the details of the hardware design for IDT drivers. Section IV presents our experimentally validated velocity model for droplets of different sizes. Section V describes the synthesis flow in more detail. Section VI presents experimental results using fabricated devices, and presents simulation results of fault-tolerant synthesis for three real-life laboratory protocols. Finally, Section VII concludes the paper. Additional details are presented in Appendix A and Appendix B.

# II. PRELIMINARY SYSTEM-LEVEL DESIGN

In this section, we describe the preliminary hardware design of the acoustofluidic biochip. We also highlight the drawbacks of this design.

# A. Hardware-Design Levels

The design of the digital acoustofluidic platform includes three design levels:

- 1) Device-level design: When an IDT is actuated, an electrical signal is transformed to an acoustic wave. Next, this acoustic wave generates refluxes (in the oil) that is then used to move the droplets [13], [20].
- 2) System-level integration: The hardware design steps that involve the assembly of IDTs to a printed-circuit-board (PCB), the generation of actuation signals, and the manipulation of the on/off status for each IDT, are collectively referred to as the integrated system-level design.
- 3) Control-software optimization: Droplet operations require precise actuations of multiple IDTs in a short period of time. Control software is used to first transform a sequence of droplet operations in the bioassay to an actuation sequence of IDTs. Next, the actuation sequence is applied to the integrated system to implement the bioassay on the biochip.

# B. Preliminary Design

A preliminary system-level design is shown in Fig. 2(a). A function generator along with a microwave amplifier is used to

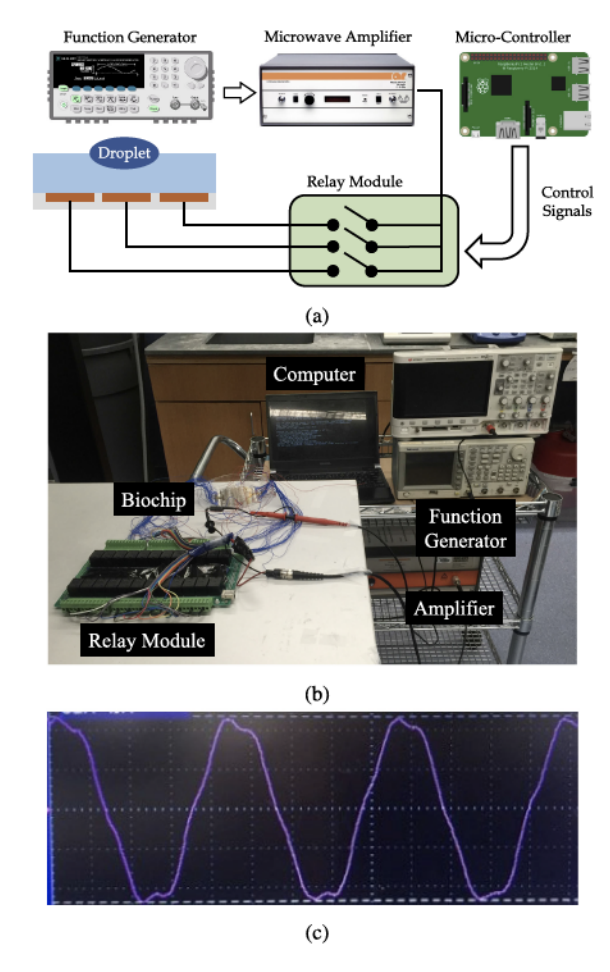


Fig. 2. Original digital acoustofluidic system: (a) system design; (b) experimental setup; (c) the waveform of the actuation signal after it goes through the relay.

generate a 24 MHz sinusoidal signal with a voltage range of  $\pm 10/\pm 20$  V. This signal is connected to a mechanical-relay module, and the close/open status of each relay in the module is controlled by a micro-controller using digital signals. When a relay is closed, the actuation signal can pass through and actuate the corresponding IDT. Otherwise, the signal is cut off, and the corresponding IDT is not actuated.

However, this system-level design suffers from three key problems:

- 1) The use of the function generator and microwave amplifier makes the experimental setup bulky, and the microwave amplifier is especially expensive.
- 2) When the output of the amplifier is set to 20 Vpp (peak-topeak voltage), the amplitude of the signal received by an IDT is reduced to 12 Vpp, and severe distortion is also observed in the signal waveform (see Fig. 2(c)).

The output impedance of the signal source is 50  $\Omega$ , but the combined measured impedance of the jump wire and the mechanical relay is  $180\,\Omega$ . Therefore, if we use the jump wire and the mechanical relay to transmit the signal, impedance mismatch will make signal bounce back.

3) When a relay in the relay module is closed, a sinusoidal signal of 12 Vpp goes through the relay to the input terminal of

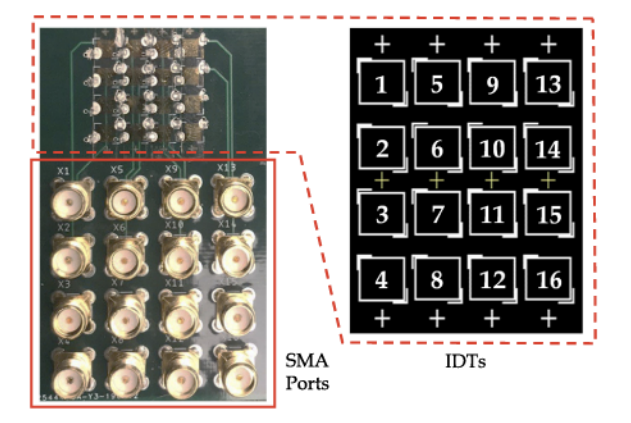


Fig. 3. Illustration of a fabricated acoustofluidic biochip.

an IDT. In this case, a sinusoidal signal of 7 Vpp is observed in the neighboring relay, which only partially actuates the corresponding IDT. Because the mechanical relay does not have a signal shielding structure (e.g., the ground shield in the outer part of a coaxial cable), the signal that goes through a relay leaks to a neighboring relay due to the signal-coupling effect.

#### III. PROPOSED SYSTEM-LEVEL DESIGN

In this section, we describe the hardware design of the acoustofluidic biochip and the IDT-driver board.

# A. The Acoustofluidic Biochip

A fabricated acoustofluidic biochip with 16 IDTs is shown in Fig. 3. We can see that all the 16 IDTs are assembled in the top area of the PCB board. Each IDT has two terminals: an RFIN terminal and a GND terminal. The GND terminal of each IDT is connected to the ground plane of the PCB board, and the RFIN terminal of each IDT is connected to an SMA port that is optimized to transmit/receive high-frequency signals. The numbering of the IDTs in the biochip is also shown in Fig. 3, which will be used in Section VI.B.

According to laboratory experiments, the maximum distance that this reflux can reach is slightly larger than the distance corresponding to the length of two-IDT distance [21], [22]. The "pitch" between IDTs influences the time need to move a droplet from one IDT to another IDT. For example, if we increase the pitch, it would take more time to move a droplet from an IDT to a neighboring IDT. Therefore, the pitch should be as small as possible. However, the minimum pitch between IDTs is determined by the dimension of the IDT. In our implementation, the dimension of an IDT is 4 mm  $\times$  4 mm. Ideally, the minimum pitch is equal to 4 mm. However, since we need to use epoxy to connect an IDT to the PCB board, the pitch is 5 mm in the actual design.

# B. The IDT-Driver Unit

In an acoustofluidic biochip, each IDT unit is driven by custom circuitry (referred to as an IDT-driver unit). As shown in Fig. 4, an IDT-driver unit includes a fanout buffer, two

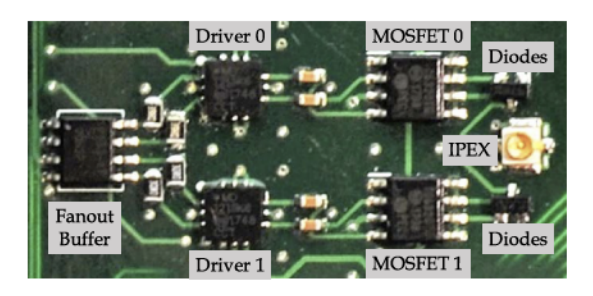


Fig. 4. Detailed layout of an IDT-driver unit.

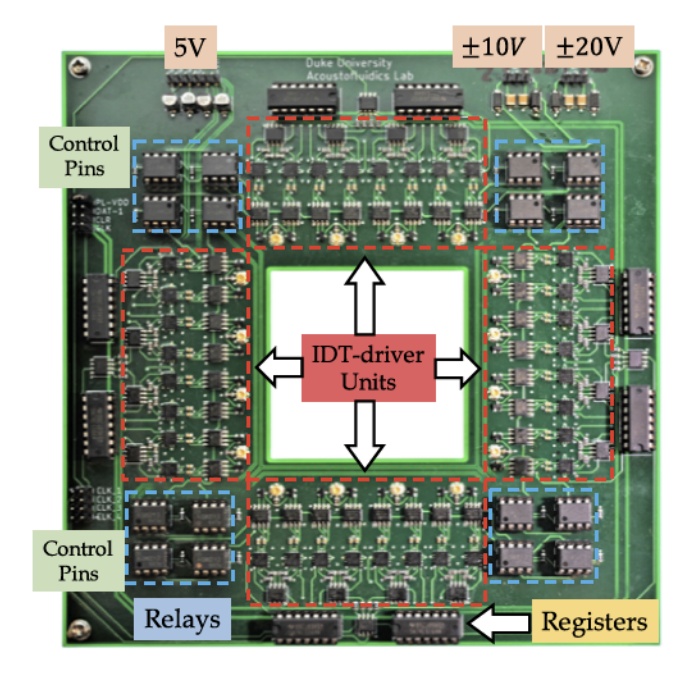


Fig. 5. Detailed layout of the IDT-driver board.

MOSFET drivers, two MOSFETs, and one IPEX interface. The fanout buffer (Part No. Microchip PL133) is used to generate high-quality 24 MHz reference signals needed by the MOSFET drivers. The combination of the MOSFET driver and the MOSFET can output a signal of frequency 24 MHz and amplitude  $\pm 10/\pm 20\,$  V. In this layout, we use two sets of MOSFET drivers and MOSFETs because the power consumption for each MOSFET is high (about 1 W). If the MOSFET operates for longer than 10 s, it will be permanently damaged because of excessive heat accumulation. In this case, the solution of two sets of hardware allow us to alleviate the heat accumulation problem by alternatively using one of the hardware components. Finally, the IPEX interface on the right is used to transmit high-frequency signals.

#### C. The IDT-Driver Board

An IDT-driver board is used to drive all IDTs in an acoustofluidic biochip. Since 16 IDTs are assembled in the biochip, the IDT-driver board should have 16 IDT-driver units, which are marked as yellow rectangles in Fig. 5. Three DC power supply rails are located in the top area of the board: 5 V for chip

TABLE I
A COMPARISON BETWEEN TWO HARDWARE SOLUTIONS

Component	Original	Proposed	
/ Parameter	Hardware Design	Hardware Design	
Connection Interface	Pin Head IPEX/SMA		
Connection Cable	Jump Wire Coaxial Cable		
PCB Routing	Normal Wire Transmission		
RF Impedance	N/A	/Α 50 Ω	
Signal Source	Function Generator FPGA Boa		
Amplifier	Bulky RF Amp IDT-Drive		
Signal Loss	50%	15%	
Signal Coupling	30% 0%		
Power Consumption	4 W per IDT 1 W per ID		
Response Time	20 ms < 0.1 ms		

operation,  $\pm 10/\pm 20$  V for the MOSFETs to generate 24 MHz and  $\pm 10/\pm 20$  V signals. Because only one of the  $\pm 10$  V and the  $\pm 20$  V DC power supplies can be connected to a MOSFET at a time, the switching between these two power supplies is implemented by solid-state relays (Part No. Panasonic AQW210) shown as blue rectangles. In addition, two control pin heads are located on the left of the chip, and the control bits are stored in the eight register chips that are located at the boundary of the board.

#### D. A Comparison Between Two Solutions

A comparison between the original solution and the proposed solution is shown in Table I. The original solution does not use transmission line or coaxial cables to deliver the 24 MHz signals, therefore 50% of the signal amplitude is lost, and 30% of the signal amplitude are coupled to neighbouring IDTs due to wire coupling effect; see row 8 and row 9 in Table I. For example, if the signal amplitude from the source is 40 Vpp, then only 20 Vpp is received by the IDT and 12 Vpp is coupled to neighbouring IDTs. However, in our proposed hardware design, we still have a 15% signal loss due to impedance mismatch between the RF system (50  $\Omega$ ) and the IDT (150  $\Omega$ ). However, this signal loss is much lower than that in the preliminary solution. In addition, because hardware designs that are specifically for RF systems, such as transmission lines, coaxial cables and IPEX/SMA interfaces, are used to deliver the signals from the source to IDTs, no signal coupling effect is inspected in laboratory experiments.

In the original hardware solution, a mechanical relay is used to control the connectivity between each IDT and the signal source. Since the metal arm in the relay has to travel for a distance to implement the switching on/off behavior, it introduces a delay between the time when the current goes through the coil and the time when the metal arm fully travels. This delay is referred to as the response time and it is about 20 ms for most mechanical relays. This delay prevent us from precisely controlling the behavior of IDTs. In the proposed hardware solution, an IDT-driver IC is used to turn on/off each IDT. According to the data sheet, the response time for an IDT-driver IC is less than 0.1 ms, which is over 200 times smaller than that of a mechanical relay.

# IV. VELOCITY MODEL

Because the acoustofluidic platform can manipulate droplets of different sizes, a synthesis solution for these biochips must consider the impact of droplet size on droplet velocity. Therefore, we have developed an analytical model to determine the impact of droplet size on velocity. This model forms a key part of the routing component of the synthesis algorithm presented in Section V.

As shown in Fig. 7, an IDT is activated and two fluidic traps are generated above the left and right parts of the IDT. If a droplet is floating on the far left of the IDT, it will be driven to the right towards the IDT, because the reflux is flowing from left to right. The forces that drive the droplet come from two sources: (1) viscous forces within the droplet; (2) viscous drag due to droplet movement through the FC-40 oil. The nature and dynamics of these forces can be described using equations [23], [24]. However, these equations are hard to solve, and it takes a long time to accurately simulate the droplet motions using an FEM software (e.g., COMSOL) [25].

In practice, the velocity profiles for different sizes of droplets are first computed off-line. Next, these results are stored in the database. The synthesis method incorporated in the control software uses this information when it generates droplet routes. If we use FEM software to obtain the velocity profiles, it will take a tremendous amount of time, and is therefore not practical.

It is reported in [26] that a semi-empirical model is used to describe droplet motion in an EWOD-based microfluidic biochip, and the resultant prediction is accurate. Therefore, we can use the simplified algebraic expressions in [26] to describe the forces appears in our simplified model. The computation of the simplified model is fast, the experimental results show that our model is also accurate.

In the simplified velocity model, the droplet is viewed as a spherical object floating on the fluorinated oil, and we assume that half of the sphere is immersed in the oil and the other half is above the oil surface. Note that this assumption is made because of the following two reasons:

- 1) The density of FC-40 is 1.85 g/mL, which is approximately twice the density of water density of water (i.e., 1 g/ml). Therefore, it is reasonable to assume that half of the droplet immerses in the FC-40 oil in the simplified model.
- 2) Consider the deformation of a droplet due to gravitational force. The surface tension of FC-40 is 16 dynes/cm (i.e.,  $1.6 \times 10^{-2}$  N/m, and the force due to surface tension on a droplet with a radius of 0.5 mm can be estimated as:

$$F \approx \pi R^2 \gamma \times \left(\frac{1}{R} + \frac{1}{R}\right) = 5.024 \times 10^{-5} \text{ N} \qquad (1)$$

where  $\gamma$  is the surface tension of FC-40 and R is the radius of the droplet.

The gravitational force on the droplet is computed as:

$$G = \rho \times \frac{4}{3}\pi R^3 \times g = 5.212 \times 10^{-6} \text{ N}$$
 (2)

where  $\rho$  is the density of water and R is the radius of the droplet.

Because the force caused by surface tension is about 10 times larger than the gravitation force, therefore droplet deformation due to the gravitational force can be neglected in the simplified

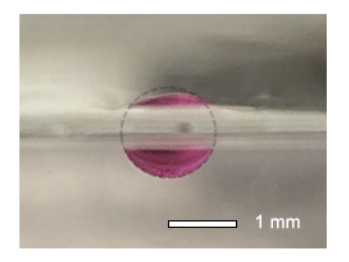


Fig. 6. Cross-section view of a droplet on the FC-40 oil.

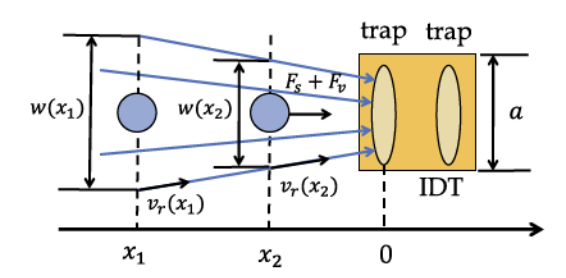


Fig. 7. Droplet undergoing transportation by an IDT.

model. In addition, gravity does not contribute to any resistance force [26]. Therefore, it is not considered in the next subsection.

Fig. 6 shows the cross-sectional view of a droplet floating on the FC-40 oil. It can be seen that half of the droplet is immersed in the FC-40 oil, and the shape of the droplet is a sphere, which validates the assumption we have made.

## A. Model Construction

As shown in Fig. 7, suppose  $x_1$   $(x_1 < 0)$  and  $x_2$   $(x_2 < 0)$  are two positions on the left side of the IDT, and the width and velocity of the reflux at position  $x_1$  and  $x_2$  are  $w_r(x_1)$ ,  $v_r(x_1)$ ,  $w_r(x_2)$  and  $v_r(x_2)$ , respectively. Because the total amount of liquid (product of width and velocity) flowing through positions  $x_1$  and position  $x_2$  are the same, we have the following equation:

$$v_r(x_1) \times w_r(x_1) = v_r(x_2) \times w_r(x_2)$$
 (3)

where the left side (right side) represents the amount of liquid flowing through position  $x_1$  ( $x_2$ ) per time unit.

Reflux Velocity: As shown in Fig. 7, the width of the reflux becomes shorter when we go from the far field to the trap; therefore, the velocity in the near-field reflux (nearer to the trap) is higher. Suppose the width of the trap is a (approximately equal to the width of an IDT) and the velocity of reflux at the trap is  $v_r(0)$  (the position is labeled as "0"). Then the reflux velocity at any given position x is given by:

$$v_r(x) = \frac{v_r(0) \times a}{w_r(x)} = \frac{v_r(0) \times a}{a + k|x|}$$
 (4)

where k is the rate of increase of the reflux width. In order to simplify the model, we assume that the reflux width increases linearly with x. Therefore, the reflux width at position x is given by a+k|x|.

Shear Force: If we assume a velocity profile in the droplet with zero-slip boundary conditions at the bottom of the droplet [26], a conservative estimate for the shear stress can be obtained

Parameter	Value	
Droplet viscosity, $\mu_d$ (water)	$8.9 \times 10^{-4} \text{ Pa}\cdot\text{s}$	
Drag coefficient, $C_d$	30	
Droplet density, $\rho_d$	$1 \times 10^3 \text{ kg/m}^3$	
FC-40 oil density, $\rho_r$	$1.9 \times 10^3 \text{ kg/m}^3$	
Reflux width increasing rate, $k$	3/m	
Reflux velocity at the trap, $v(0)$	$2.2 \times 10^{-3} \text{ m/s}$	
IDT/trap width, a	$5 \times 10^{-3} \text{ m}$	

TABLE II PARAMETERS USED FOR MODEL VALIDATION

by assuming a parabolic velocity profile. The total shear force exerted by the fluorinated oil can be expressed as:

$$F_s = \frac{6\mu_d(v_r - v_d)}{2r} \times \pi r^2 = 3\mu_d \pi r \times (v_r - v_d)$$
 (5)

where  $u_d$  is the droplet viscosity, r is the radius of the droplet,  $v_r$  is the reflux velocity, and  $v_d$  is the droplet velocity.

Viscous Drag Force: Assuming that the droplet is moving through the fluorinated oil as a rigid body (this is a valid assumption because the reflux is faster than the droplet [13], [20]), the viscous drag force can be estimated by the following equation:

$$F_v = 0.5 \times (C_d \rho_r (v_r - v_d)^2) \times (2r^2)$$
  
=  $C_d \rho_r r^2 (v_r - v_d)^2$  (6)

where  $C_d$  is the drag coefficient for a cylinder in a cross flow and  $\rho_r$  is the density for reflux (i.e., fluorinated oil).

Based on above analysis, the equation governing the droplet motion can be written as:

$$m\frac{d^2x}{dt^2} = F_s + F_v \tag{7}$$

Note that Equation (7) is described using a one-dimensional coordinate system (see Fig. 7). Given that the trap is located at the origin, and the positive direction is from left to right, the location of a droplet can be fully described using the coordinate x. Therefore, x is the coordinate of a droplet in the one-dimension coordinate system modeled in Fig. 7. In addition, m is the mass of the droplet and the variable  $v_d$  in  $F_s$  and  $F_v$  can be expressed in the form of dx/dt. Assume that at t=0, the droplet position  $x=-5\times 10^{-3}$  m, and the droplet velocity is dx/dt=0 m/s. This ordinary differential equation (ODE) is solved using MATLAB [27], and the source code can be viewed and downloaded from [28].

# B. Model Validation

The above velocity model was validated experimentally. The parameters used for model validation, listed in Table II, are based on a fabricated acoustofluidic biochip and the characterization done with it. Experiments on droplets of radii  $r=0.7\,\mathrm{mm}$  and  $r=1.1\,\mathrm{mm}$  were performed in the laboratory on a  $4\times4$  acoustofluidic biochip.

A comparison between the analytical and experimental results is shown in Fig. 8. Note that the reference point in Fig. 8 is actually the location of the trap. We conclude that there is a

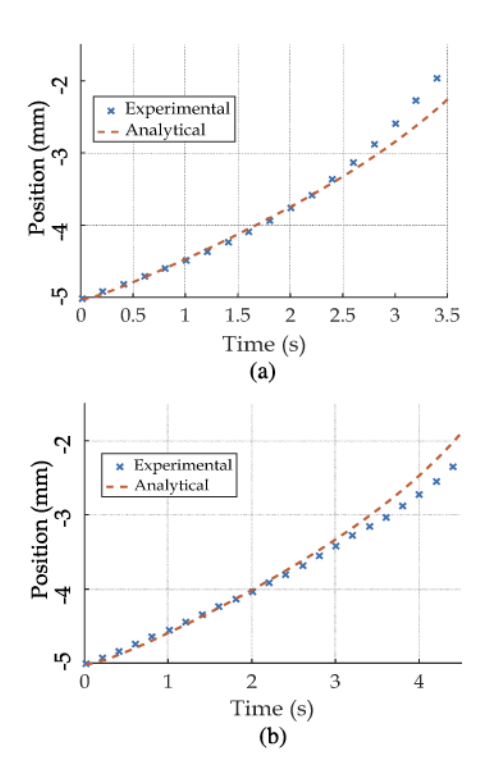


Fig. 8. Comparison between analytical and experimental results (distance versus time) for a droplet of radius (a) 0.7 mm and (b) 1.1 mm.

good fit between the analytical and experimental results, which highlights the accuracy of the proposed velocity model.

#### V. FAULT-TOLERANT SYNTHESIS

In this section, we develop a synthesis method for the acoustofluidics platform based on [14]. There are two major differences between the proposed method and the method in [14]:

- The acoustofluidic biochip is inherently fault-tolerant with respect to droplet movement. We utilize this property to tolerate faulty IDTs.
- Fluidic modules on the acoustofluidics platform have a direction property. We utilize this characteristic to implement droplet routing and module placement in a more time- and space-efficient manner.

Note that both trap locations (Fig. 7) for each IDT are considered in our high-level synthesis algorithm.

# A. Problem Formulation

We are given a reconfigurable  $W \times H$  acoustofluidic biochip. Each IDT is identified by its coordinate (x,y) with the origin (0,0) at the top-left corner.

Input: (1) The sequencing graph G=(V,E) that represent the bioassay, where V represents fluidic operations and E represents the dependencies between all pairs of operations; (2) The acoustofluidic biochip library, which includes the type, size and corresponding execution time of on-chip fluidic functional modules; (3) The size of the acoustofluidic biochip (e.g., the  $W \times H$  IDT array). (4) The list of faulty IDTs on the acoustofluidic biochip.

*Objective:* Minimize the bioassay completion time.

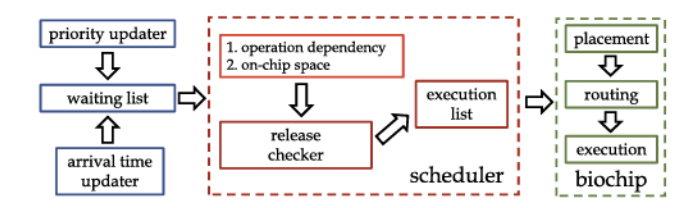


Fig. 9. Illustration of the synthesis technique.

#### B. Scheduling Technique

Fig. 9 describes the synthesis technique (expanded from [14]) used for the acoustofluidic biochip. First, all fluidic operations are loaded into the waiting list. The order of operations is determined by the arrival-time updater and the priority updater. The values of the arrival time and the priority for each operation in the waiting list are obtained based on the sequencing graph of unscheduled operations. Therefore, they are refreshed when any operation in the waiting list is fed to the scheduler. When an operation from the waiting list arrives at the scheduler, the release checker determines whether this operation can be carried out on the chip at the current time. For a fluidic operation, the following two conditions are examined: (1) Operation dependency. Parent operations should be completed before we can carry out this operation; (2) On-chip space. The target operation can be carried out only when there is enough space on the biochip. If both C-1 and C-2 are satisfied, the newly arrived operation is placed in the execution list and carried out at the current time.

# C. Motivational Example

According to [29], an IDT can fail in the IDT-fabrication process, in the IDT-PCB integration process, or during the execution of the bioassay. The reasons for failure include shorted-pin defects, dielectric-breakdown defects, and open RFIN-pad defects. Because the IDT-array based biochip is still in an early prototype stage in terms of technological maturity, all the fabrication steps are still implemented manually in a university laboratory setting. For a biochip with a  $4\times4$  IDT array, 50% of the biochip contains faulty IDTs. In fact, based on our inspection in the lab, there are at most three faulty IDTs in a newly fabricated 4X4 IDT array.

For the lab-on-chip applications considered in [13], [20], a  $6 \times 6$  or larger IDT array is needed. With a larger number of IDTs, we can implement more complex bioassays, or run more tests in parallel. An additional motivation for larger arrays is that the hardware cost (especially the IDT-driver circuit) scales (goes down) with the number of IDTs. Recent developments related to the COVID-19 pandemic have also shown that rapid testing through parallelism is highly desirable.

Although the yield of the biochip (i.e., the IDT array) can be improved through commercialization and better process technologies. However, as the utilization of an IDT increases, the performance of an IDT degrades due to IDT surface contamination and wear-out. In some situations, dielectric breakdown occurs in an IDT, and this phenomenon has been reported in [29]. If the performance degradation is beyond the acceptable (calibrated) range, the corresponding IDT is regarded as a "faulty IDT" and considered in the proposed fault-tolerant synthesis algorithm.

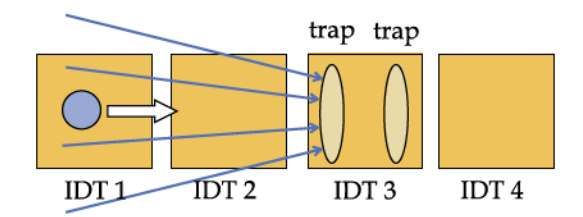


Fig. 10. Illustration of fault-tolerance capability.

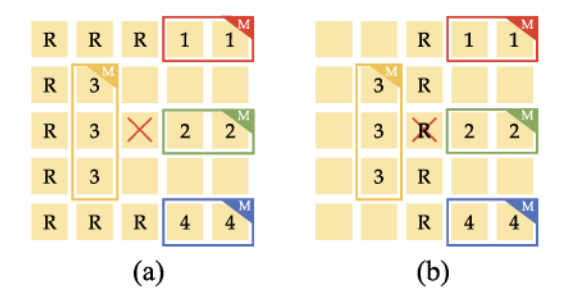


Fig. 11. Motivational example of a biochip (a) without fault tolerance, and (b) with fault tolerance.

Note that if an IDT is faulty, it cannot function properly, e.g., the IDT cannot be actuated and there is severe performance degradation. A method that can be used detect faulty IDTs integrated on a PCB board is reported and validated in [29]. One of the unique features of an acoustofluidic biochip is its inherent fault tolerance — the reflux of an IDT can reach a distance of two IDTs. As a result, if an IDT is faulty, we can still move a droplet through the faulty electrode using the far-field reflux (see [21] for a video demonstration of an experiment that we have carried out).

As the utilization of an IDT increases, the performance of an IDT gradually degrades due to surface modification. However, until now, no method has been reported to detect and handle the performance degradation of IDTs. Therefore, IDTs with gradual performance degradation are not discussed in this paper.

An example for the fault-tolerant feature is illustrated in Fig. 10: a droplet is floating on top of IDT1 and IDT2 is faulty. In this case, if IDT3 is activated, a reflux that can reach as far as IDT1 is generated, and the droplet on IDT1 can be moved from IDT1 to IDT3 without the need to activate IDT2. However, because the far-field reflux velocity is relatively low, it takes longer time for the droplet to move from IDT1 to IDT2. Note that if two consecutive IDTs are faulty (e.g., both IDT2 and IDT3 are faulty), the droplet on IDT1 cannot be moved to IDT4 by actuating IDT4. In this case, the droplet has to take a detour to reach IDT4.

Suppose we have a  $5 \times 5$  acoustofluidic biochip, and one of the IDTs is faulty (denoted by red cross in Fig. 11). Suppose at time t, four fluidic modules (M-1, M-2, M-3 and M-4) are placed on the biochip, and the droplet of M-1 (top right corner) needs to move to M-4 (bottom right corner). As shown in Fig. 11, if this biochip does not have fault tolerance, the droplet needs to use a relatively long route to reach M-4 (denoted by "R"). However, if this biochip is fault-tolerant, the droplet can reach M-4 using a much shorter route that goes through the faulty IDT. Suppose the

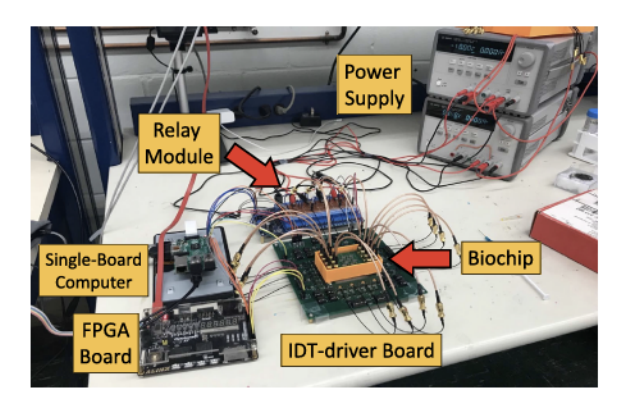


Fig. 12. Illustration of the system setup.

times needed to move through a fault-free and a faulty IDTs are 0.5 s and 1 s, respectively. Then, the routing time for the first case and the second case are 5 s and 3.5 s, respectively. Therefore, we can use the inherent fault tolerance of this platform to reduce the routing time in the presence of faults, and thereby reduce the overall bioassay execution time.

Additional details of the fault-tolerant high-level synthesis method are included in Appendix B.

#### VI. EXPERIMENTAL RESULTS

In this section, we present the hardware setup and the experimental results for droplet routing and an example bioassay.

#### A. Hardware Setup

The hardware setup used to operate an acoustofluidic biochip is shown in Fig. 12. We can see that the acoustofluidic biochip is installed in an orange plastic holder, and they are together placed at the centre of the IDT-driver board. The IPEX interface from each IDT-driver unit is connected to an SMA port in the biochip through a coaxial cable (50 ohm impedance). Two bench-top DC power supplies provide the desired DC voltages for the IDT-driver board. The upper power supply generates 5 V for chip operation and provides a  $\pm 10$  V power rail for IDT-driver board to generate a 20 Vpp signal. The lower power supply provides a  $\pm 20$  V power rail for IDT-driver board to generate a 40 Vpp signal. A single-board computer (Raspberry Pi) on the left is used to send control signals to the IDT-driver board.

The system presented here does not have a top cover, which brings benefits such as easy sample addition and collection while leading to challenges related to droplet evaporation, especially for droplets at the nanoliter-scale. However, due to the low surface tension of FC-40 oil (16 dynes/cm), the FC-40 oil will spontaneously wet on the water droplets (72 dynes/cm) as an immiscible coating layer against evaporation. It is reported in [22] that after an incubation period of 58 minutes, the volume of the droplet is reduced by less than 5.8%.

In addition, it is possible to develop a control system that can maintain the air humidity so as to further minimize the evaporation of water droplets. This approach is used in [30], where aqueous droplets are manipulated for cell transfection in air using acoustic levitation.

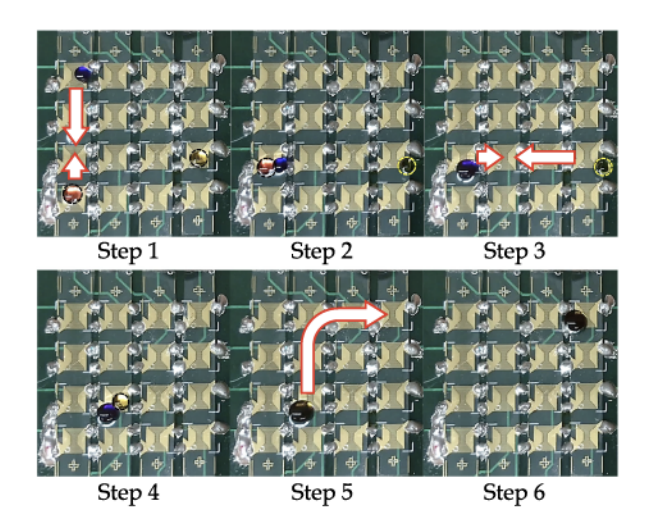


Fig. 13. Experimental demonstration of a simple bioassay.

Although there is no surfactant in the oil to maintain the surface tension barrier, the draining of the oil-film between the two nL-level droplets may take up to several seconds. In order to accelerate the droplet-mixing process, according to [30], opposite charges are assigned to the two droplets that are going to mix when they are dispensed.

# B. Experimental Demo for System Design

The experimental demonstration of using a droplet to write four letters of "DUKE" is shown in Fig. 14. This experiment shows the accurate droplet-control capability of the acoustofluidic biochip. In the second experiment, we carry out a simple bioassay in the acoustofluidic biochip. In this experiment, a CCD camera was used to capture the video, and the images for each step is extracted from the recorded video and shown in Fig. 13. At first, droplet A (blue), droplet B (red) and droplet C (yellow) are located at IDT-1, IDT-4 and IDT-15, respectively (refer to Fig. 3 for IDT numbering). Next, droplet A and droplet B are merged at IDT-4, and the merged droplet is then merged with droplet C at IDT-7. Finally, the outcome droplet is transported to the exit (IDT-13). The experiment demonstration videos can be viewed and downloaded from [31], [32].

Note that the thickness of the connecting epoxy is approximately 1 mm. This thickness does not affect droplet movement because the liquid level is about 4 mm. In this case, the maximum radius of the droplet can be 3 mm.

# C. Simulation Results for Fault-Tolerant Synthesis

We use three real-life benchmarks, namely CEP, serial dilution, and master mix [33] for evaluation; see Fig. 15. CEP is a combination of three small bioassays: cell lysis, mRNA extraction, and mRNA purification. The synthesis method for MEDA DMFBs [14] is used as a baseline for comparison. For the baseline method, the spacing between each module and a route is at least one IDT. All simulations are carried out on an Intel Core i5 platform with a 2.70 GHz CPU and 8 GB of RAM. We use a  $5\times 5$  IDT array. The fluidic module library used for the digital acoustofluidic platform is shown in Table III. The

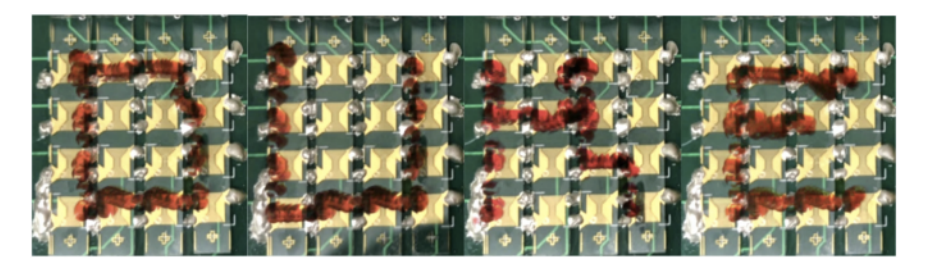


Fig. 14. Time-lapsed droplet trajectory for writing the letters of "DUKE" (the time interval is 2 s).

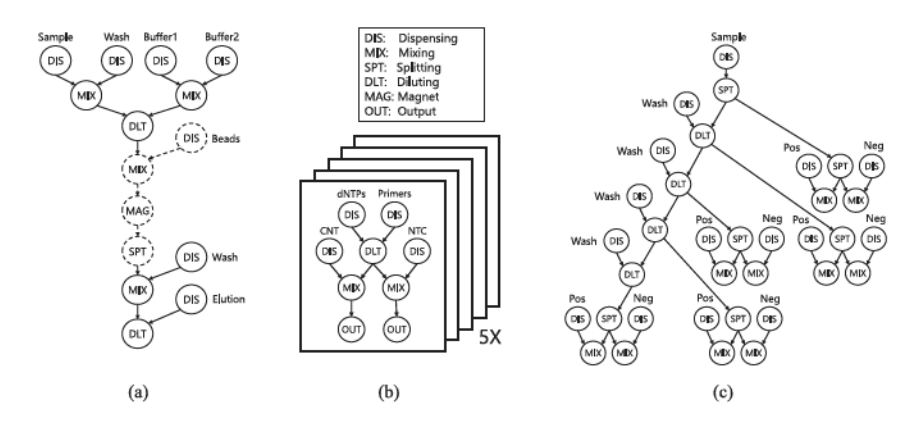


Fig. 15. (a) CEP benchmark, (b) the master-mix benchmark, and (c) the serial-dilution benchmark.

TABLE III EXPERIMENTALLY CHARACTERIZED MODULE LIBRARY FOR SYNTHESIS

Architecture	Operation	Resource	Time	
Acoustofluidic Biochip	Dispensing	Reservoir	3 s	
	Mixing	1 × 2-array mixer	3 s	
		$2 \times 1$ -array mixer	ay mixer	
	Splitting	$1 \times 3$ -array splitter	2 s	
		3 × 1-array splitter		
	Diluting	$1 \times 3$ -array diluter	5 s	
	Diluting	$3 \times 1$ -array diluter	3 3	

dispensing time for the reservoir was 3 s. The mixing time was 3 s for both  $1 \times 2$  and  $2 \times 1$ -array mixers. The splitting time was 2 s for both  $1 \times 3$  and  $3 \times 1$ -array splitters. Finally, the dilution time was 5 s for both  $1 \times 3$  and  $3 \times 1$ -array diluters.

We evaluate fault tolerance on the basis of droplet routing time and bioassay completion time. We randomly inject up to six faulty IDTs into each benchmark and simulate it 100 times. Then, we calculate the average routing time and average completion time for the proposed method and the baseline method.

Fig. 16(a) shows the relationship between the normalized completion time for three bioassays with no faulty IDT and penalty factor p. The normalized completion time is the ratio of the completion time between the proposed method and the baseline method. Because the completion time for the baseline method is always larger than the proposed method, this ratio is always less than 1. Our results show that lower normalized completion time can be achieved for a low value of p for serial

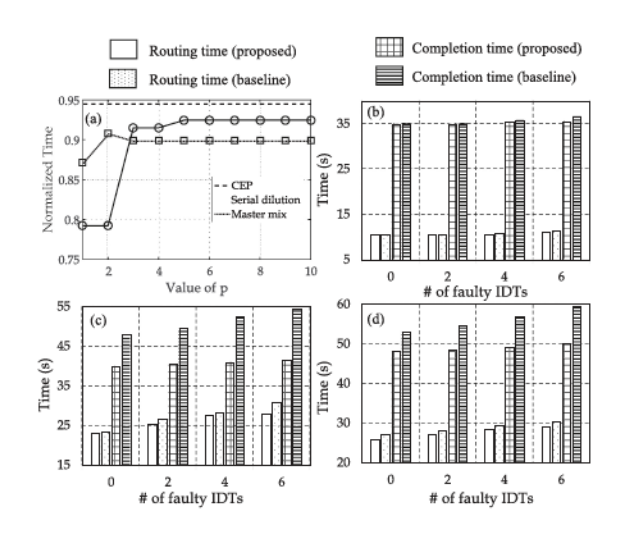


Fig. 16. (a) Normalized completion times for three bioassays. The routing times and completion times for (b) CEP, (c) serial dilution and (d) master mix bioassays.

dilution and master mix. However, the normalized completion time remains constant for CEP with p, because the biochip is relatively large for this bioassay.

Fig. 16(b)–(d) present simulation results on the completion time and routing time of each benchmark when 0, 2, 4 and 6 faulty IDTs are randomly injected. The routing time and completion time using the proposed fault-tolerant synthesis algorithm are consistently less than that obtained using the baseline method for two benchmarks. For the smallest benchmark (i.e., CEP),

there is little difference between the two methods, because the biochip is comparatively large for the bioassay. Even when some of the IDTs fail, there are sufficient resources (i.e., IDTs) available for module placement and droplet routing. However, for the two larger benchmarks, the gap in completion times keep increasing as the number of faulty IDTs increases. For the baseline method, the failure of some IDTs forces droplets to wait until on-chip resources are released by fluidic modules. However, in the proposed method, because of the inherent fault tolerance of acoustofluidics, a route can pass through some of the faulty IDTs, which is not available for conventional DMBs.

When sample incubation is carried out in benchtop assays using large instruments, the liquid volumes are large and hence more time is needed for these operations. As these assays are scaled down to acoustofluidic biochips, the time required for incubation is also expected to be reduced—commensurate with the reduction in liquid volumes. Therefore, the impact of time reduction for on-chip pre-concentration, sample preparation, pre-incubation steps, and droplet routing will have a significant impact on the time-to-response. In addition, the control software allows us to parallelize the sample preparation steps before incubation and the final step when samples are presented to detectors for sensing. According to [34], sample preparation accounts for 90% of the cost and 95% of the analysis time in biochemical experiments.

#### VII. CONCLUSION

We have presented a hardware design that can effectively operate an acoustofluidic biochip. Compared with a preliminary hardware solution, it has three major advantages: (1) smaller form factor and lower cost; (2) effective and high quality signal generation and transmission; (3) fully-automated and flexible biochip control. Experimental demonstrations of accurate droplet movements and a bioassay execution have shown the effectiveness of our hardware design. In addition, we have presented a fault-tolerant synthesis technique that allows us to automatically map biomolecular protocols to an acoustofluidic biochips. We have derived and experimentally validated a droplet velocity model, and used it to guide co-optimization for operation scheduling, module placement, and droplet routing in the presence of IDT faults. We have presented experimental results using fabricated acoustofluidic biochips and simulation results for benchmark protocols to demonstrate the effectiveness of the proposed solution. Our results are expected to open new research directions on design automation of digital acoustofluidic biochips.

# APPENDIX A ACOUSTOFLUIDIC BIOCHIPS

#### A. Fabrication of an IDT

A photoresist layer is first coated on a LiNbO<sub>3</sub> substrate (from Precision Micro-Optics, USA) using spin-coating process (Step 2); see Fig. 17. Next, the substrate is exposed under a UV light with a photomask cover (Step 3). In this case, part of the substrate area is exposed to UV light while the other area is shaded by

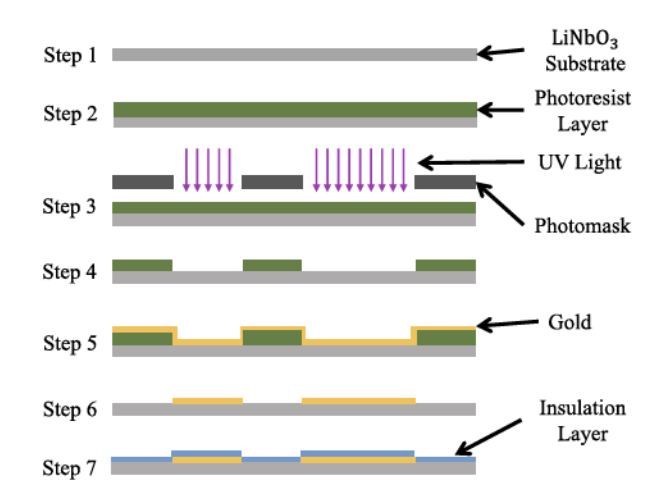


Fig. 17. Fabrication process of an IDT.

the photomask. After that, a chemical etching process is used to wash out the photomask in the area that is directly exposed in UV light (Step 4). An E-beam gold evaporation process is then used to deposit a 5 nm Cr/50 nm Au layer on the top (Step 5). After the remaining photoresist layer is peeled off, a golden pattern of IDT is left on the substrate (Step 6). Finally, a 8  $\mu$ m SU-8 photoresist layer is coated on the top as the insulation layer (Step 7 is optional). In the experimental setup, there is no insulation layer on top of the IDT because the FC-40 oil is not conductive.

However, if distilled water instead of FC-40 is used, then an 8  $\mu m$  SU-8 photoresist layer can be used to electrically isolate the water from the IDT. Note that 8  $\mu m$  is the minimum thickness of the SU-8 photoresist layer that can be achieved in the lab environment, i.e., easy to fabricate and of good durability. Other material such as SiO\_2 and LiNbO\_3 can also be utilized, but the SiO\_2 layer is more vulnerable to dielectric breakdown if the thickness is less than 8  $\mu m$ , and the LiNbO\_3 layer can be easily shattered when the IDT array is baked in the oven. Therefore, SU-8 is deemed to be the best choice for the insulation layer. The existence of the SU-8 photoresist layer will have an impact on the performance of an IDT. However, based on experimental results, the performance degradation due to the photoresist layer is very small.

# B. Fabrication of a Biochip

After multiple IDTs are fabricated, we need to assemble them on a PCB board, and the steps are shown in Fig. 18. First, each IDT is cut along the boundary of the golden pattern (Step 1). Next, the IDT is aligned to the PCB board (Step 2), and silver epoxy (from MG Chemicals, USA) is used to connect the terminals of the IDT to the corresponding pads on the PCB board. After that, the whole PCB board is put into a oven and it is baked at a temperature of 65 °C for one hour (Step 4). Finally, we obtain the biochip as shown in Fig. 3.

# C. Directionality of IDT Activation

Each IDT has two working modes, namely the x-mode and the y-mode. As shown in Fig. 1(c), when an IDT is activated

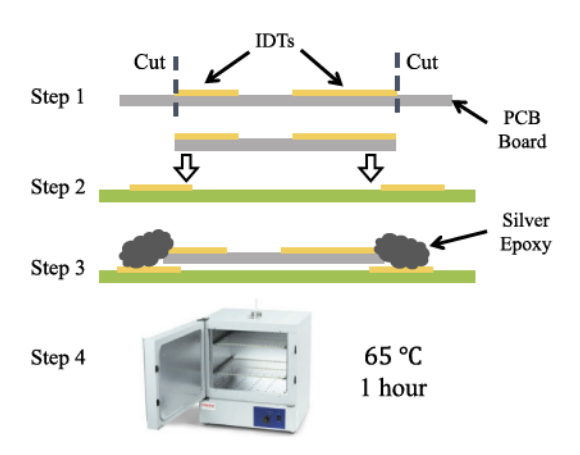


Fig. 18. Fabrication process for an IDT array.

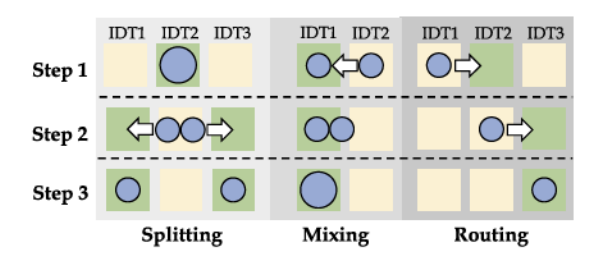


Fig. 19. The on/off states of each IDTs for droplet splitting, mixing and routing operations.

with a signal of 24 MHz and  $\pm 10$  V (i.e., x-mode), the traps are located on the left and right sides of the IDT, and the refluxes are along the x-axis. On the other hand, when an IDT is activated with a signal of 24 MHz and  $\pm 20$  V (i.e., y-mode), the traps are also located on the left and right sides of the IDT, but the refluxes are along the y-axis.

#### D. Reconfigurability

An acoustofluidic biochip is essentially an array of IDTs, and it allows dynamic grouping of IDTs to form different fluidic modules. Fig. 19 shows IDT grouping and the on/off sequence for each IDT. In the droplet-splitting module, IDT2 is first activated to generate an upward fluidic pulse and then tear the droplet into two parts. Next, IDT1 and IDT3 are activated to separate the two split child droplets. In the droplet-mixing module, two droplets are first distributed on IDT1 and IDT2, respectively. Next, IDT1 is activated, which drives the droplet on IDT2 to IDT1 and makes the two droplets merge. In the droplet-routing module, suppose the droplet on IDT1 needs to be moved to IDT3. In this case, we need to activated IDT2 and IDT3 sequentially.

The automated use of the acoustofluidic biochip is shown in Fig. 20. First, the sequencing graph of the bioassay is loaded into the computer. Next, the synthesizer software takes this sequencing graph as input and generates the schedule of fluidic operations and module placement of fluidic modules. Finally, the synthesis result is translated into a 0/1 sequence (or pattern) and loaded into the registers on the biochip. A combination

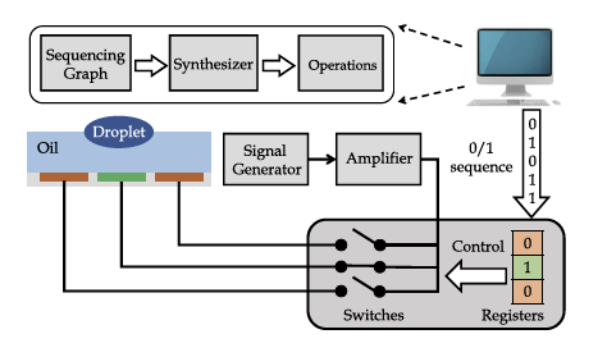


Fig. 20. Automated use of the acoustofluidic biochip.

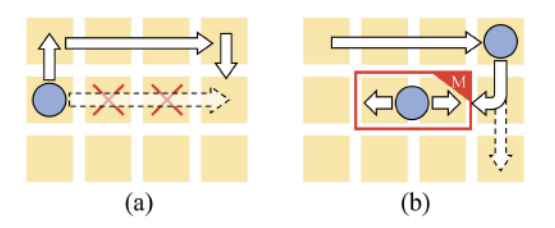


Fig. 21. (a) Routing constraint 1; (b) Routing constraint 2.

of a signal generator and an amplifier generates a signal (e.g., 24 MHz and 40 Vpp) that can activate the IDTs. The 0/1 bits loaded into the registers are used to control the on/off of the switches, and thus control the on/off state of each IDT on the acoustofluidic biochip. Therefore, by applying an appropriate 0/1 pattern to the registers, we are able to carry out fluidic operations and bioassays on the acoustofluidic biochip in an programmable manner. We have performed experiments on a fabricated acoustofluidic biochips to demonstrate these operations. Demonstration videos can be viewed from [21].

# APPENDIX B FAULT-TOLERANT SYNTHESIS

#### A. Routing Constraints

Before introducing the routing algorithm, we describe two constraints for droplet routing on a acoustofluidic biochip:

*RC-1:* A droplet cannot go through two consecutive faulty IDTs. As mentioned in Section V.C, the effective range for a reflux is only a two-IDT distance. For example, in Fig. 21(a), we assume that two IDTs in the middle are faulty. If a droplet needs as indicated it cannot move over the two faulty IDTs to reach its destination. Instead, we need to use another route.

RC-2: If the direction of a route is perpendicular to the direction of a fluidic module, the operation in the fluidic module must be paused. Otherwise, the droplets are likely to merge (see [21] for a video demonstration on our biochip). For example, in Fig. 21(b), an x-direction mixer is placed on the biochip. In this case, suppose a droplet needs to move from the top left corner to the bottom right corner. In the first section of the route (x-direction part), because the reflux generated by the mixer is in the x-direction, the droplet being routed is not affected. However, in the second section of the route (y-direction part),

```
Algorithm 1 droplet_router(start_node, end_node, p)
Input: The start node, end node, and penalty factor p;
Output: The route from start node to end node:
 1: open={}; // the set of nodes to be evaluated
2: closed={}; // the set of nodes already evaluated
 3: open.add(start_node);
 4: while true do
       current:=find_lowest_f_cost(open);
       open.remove(current); closed.add(current);
       if current=end_node then // path has been found
           return route;
 9:
       for each neighbor of current do
           if neighbor not traversable or neighbor in closed then continue;
10:
           if neighbor is faulty and current is faulty then continue;
11:
           if updated_f_cost(neighbor) < current_f_cost(neighbor) or
12:
             neighbor not in open then
13:
              neighbor.g\_cost := current.g\_cost + neighbor.\Delta cost;
14:
              if n=num_module(neighbor)>0 then neighbor.g_cost+=n \times p;
15:
              neighbor.f\_cost := neighbor.g\_cost + neighbor.h\_cost;
16:
17:
              neighbor.parent:=current;
              if neighbor not in open then open.add(neighbor)
18
```

Fig. 22. Pseudocode for the droplet router.

the movement direction is perpendicular to the direction of reflux from the mixer. As a result, the routing droplet merges with the droplet in the mixer. In this case, the mixer should wait for the routing to be completed.

Due to RC-2, if there are many module-route conflicts, the bioassay execution time will increase. An effective way to eliminate module-route conflicts is to add a "guard ring" around each fluidic module, i.e., the spacing between droplet routes and fluidic module is at least one IDT. In this case, droplet movement will no longer be affected by the reflux generated by the fluidic modules. However, this method reduces the available space for routing, and increase the overall routing time. Therefore, we need to make a trade-off between module-route conflicts and space available for routing.

# B. Droplet Routing

Our droplet router is based-on the  $A^*$ -algorithm [35]. In an acousto- fluidic biochip, each IDT can be regarded as one "node". Suppose we are given a start node and an end node. The objective is to find a route from the start node to the end node. Each node has two costs, namely G-cost and H-cost. For a node N, G-cost is the cost of a path from the start node to N. H-cost estimates the cost of a path from N to the end node. In our work, H-cost is estimated as the *Manhattan distance* between N and the end node. The F-cost is the summation of G-cost and H-cost, and the aim in the  $A^*$  is to find a path to minimize F-cost for the end node. The pseudocode for the droplet router is shown in Fig. 22. First, two node sets (open and closed) are created and the start node is added into the open set (lines 1-3). Next, the node with the lowest F-cost in the open set is selected as the current node, and it is moved from the open set to the closed set (lines 5–6). If the current node is found to be the end node, then we backtrack to the start node, and return the resultant route (lines 7–8). Otherwise, we carry out the following steps for each neighbor node:

1) If the neighbor node is occupied by a fluidic module or it is in the closed set (i.e., already evaluated), we skip to the next neighbor node. Otherwise, go to Step 2. (line 10).

- 2) If both the current node and the neighbor node are faulty IDTs (i.e., according to RC-1), we skip to the next neighbor node. Otherwise, go to Step 3. (line 11).
- 3) If the neighbor node is not in the open set (i.e., not visited before) or the F-cost derived from the current node is smaller (i.e., lower-cost path from the start node), then the information of this neighboring node is updated (lines 12–13):
  - The G-cost of the neighbor node is the summation of the G-cost of the current node and the cost of the neighbor node (line 14). Note that, the "cost" here indicate the time needed for a droplet to pass an IDT. Different size of droplets will yield different costs, and the cost for a droplet to go through a faulty IDT is larger than a fault-free one.
  - If this neighbor node is next to a fluidic module and the
    direction from the current node to the neighbor node is
    perpendicular to the direction of the fluidic module, a
    penalty is added (i.e., according to RC-2) (line 15). Here,
    function num\_module is used to count the number of
    fluidic modules that are in conflict with the route from
    current node to the neighboring node.
  - If the penalty p is small, there might be many module-route conflicts and the potential for increased completion time. However, if p is large, there will be fewer module-route conflicts. But the space left for routing is reduced, and the router is likely to find a "detour" or it must wait until an available route appears.
    - Therefore, the selection of p reflects the trade-off between two scenarios: (1) more space for routing but more module-route conflicts, and (2) less module-route conflicts but less space for routing. The relationship between p and bioassay completion time is discussed in Section VI.
  - Finally, the new F-cost of the neighbor node is obtained and the parent of this neighbour node is updated to the current node (lines 16-17).

The worst-case computational complexity of our routing algorithm is  $O(N_i^4)$ , where  $N_i$  is the number of on-chip IDTs.

#### C. Module Placement

Module placement is based on the notion of a forbidden set (FS), which refers to a set of locations where a new module  $M_i$  cannot be placed. Two constraints were used in [14] to obtain the corresponding forbidden set: (1) **PC-1**: the new module  $M_i$  cannot overlap with any placed modules, and must maintain a minimum spacing between them (at least several microelectrode on MEDA); (2) **PC-2**: the new module  $M_i$  cannot overlap with the device boundary. After the forbidden set  $FS(M_i)$  for is obtained, the possible placement set  $PS(M_i)$  (i.e., a set of locations where  $M_i$  can be placed) is given by  $PS(M_i) = U - FS(M_i)$ , where U is the universal set of all locations on the biochip.

After the placement set PS is obtained, the next objective is to determine an optimal position for placing the new module in the PS. We carry out a linear search on PS and select the optimal location with the lowest placement cost. The placement cost PC for a new module  $M_i$  is defined as  $PC(M_i) = \max_{o_j \in parent(o_i)} \{RT_{ij}(M_i, M_j)\}$ , where  $parent(o_i)$  is the set

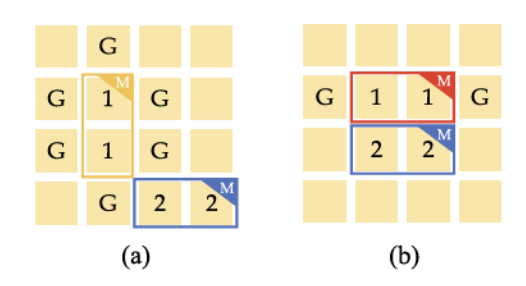


Fig. 23. Illustration of module placement.

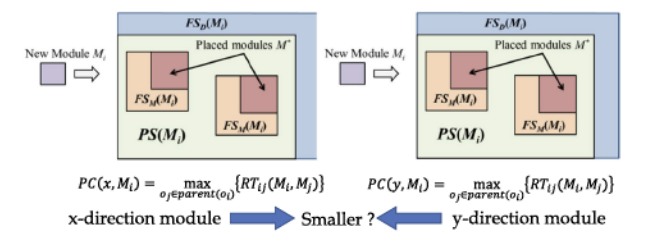


Fig. 24. Illustration of module mapping selection.

of  $o_i$ 's parent operations and  $M_j$  is the associated fluidic module for  $o_j$ .

Note that each fluidic modules should maintain at least one IDT spacing to avoid module-operation conflict. However, a key difference from MEDA is that each module has a direction property and modules with the same direction can be placed in parallel without any spacing (i.e., guard ring). Therefore, we need to modify the first placement constraint (PC-1): (1) if a placed module  $M_{p1}$  is in the same direction of the new module  $M_i$ , then  $M_i$  can be placed in parallel with  $M_p$  without any spacing; (2) if a placed module  $M_{p2}$  is in the perpendicular direction with  $M_i$ , then  $M_i$  should not cover the guard-ring of  $M_{p2}$  (one IDT in width).

An example is shown in Fig. 23. In Fig. 23(a), suppose the new module  $M_2$  is in the x direction and module  $M_1$  has already been placed. Because  $M_2$  and  $M_1$  have different directions, there is a guard ring around  $M_1$  (denoted by "G"), and  $M_2$  can only be placed in the location where it does not cover the guard ring. In Fig. 23(b), we assume that  $M_2$  is the new module and  $M_1$  has already been placed. However, because  $M_1$  and  $M_2$  have the same direction,  $M_2$  can be placed on the top and bottom of  $M_1$  without any spacing. There is still a guard ring on either side of  $M_1$ . However, compared with the former situation, the area of guard ring is now less.

Based on the modified constraints, we are able to obtain the forbidden set FS, the placement set PS, and finally the location with the minimum placement cost. On the acoustofluidic platform, there are always two module options for mixing, splitting and diluting operation (x-direction or y-direction). In order to make a decision, we apply a greedy strategy. As shown in Fig. 24, for a particular operation  $o_i$ , we first attempt to place the x-direction module and the y-direction module on the biochip individually and compute the minimum placement cost PC for each of them. The module that yields a smaller PC is selected.

#### REFERENCES

- R. B. Fair, "Digital microfluidics: Is a true lab-on-a-chip possible?" Microfluidics Nanofluidics, vol. 3, no. 3, pp. 245–281, 2007.
- [2] X. Li et al., "Magnetic timing valves for fluid control in paper-based microfluidics," Lab Chip, vol. 13, no. 13, pp. 2609–2614, 2013.
- [3] K. Chakrabarty et al., "Design tools for digital microfluidic biochips: Toward functional diversification and more than moore," TCAD, vol. 29, no. 7, pp. 1001–1017, 2010.
- [4] L. R. Volpatti et al., "Commercialization of microfluidic devices," Trends Biotechnol., vol. 32, no. 7, pp. 347–350, 2014.
- [5] S. Miller et al., "Multiplex detection of respiratory pathogens with Genmark's Eplex sample-to-answer system," Clin. Chem. Lab. Med., vol. 54, no. 5, pp. eA5–eA6, 2016.
- [6] S. Norton et al., "Development of automated enzymatic assays for NAGLU, GALNS, ARSB and TPP1 for high throughput newborn screening using digital microfluidics," Mol. Genetics Metabol., vol. 123, no. 2, p. S107, 2018.
- [7] T.-C. Liang et al., "Multi-target sample preparation using MEDA biochips," TCAD, 2019.
- [8] T.-C. Liang et al., "Programmable daisychaining of microelectrodes to secure bioassay ip in meda biochips," TVLSI, vol. 28, no. 5, pp. 1269–1282, 2020.
- [9] T.-C. Liang et al., "Execution of provably secure assays on meda biochips to thwart attacks," in Proc. Asia South Pacific Des. Autom. Conf., 2019, pp. 51–57.
- [10] T.-C. Liang et al., "Sample preparation for multiple-reactant bioassays on micro-electrode-dot-array biochips," in Proc. Asia South Pacific Des. Autom. Conf., 2019, pp. 468–473.
- [11] J.-Y. Yoon et al., "Preventing biomolecular adsorption in electrowetting-based biofluidic chips," Anal. Chem., vol. 75, no. 19, pp. 5097–5102, 2003.
- [12] H. Moon et al., "An integrated digital microfluidic chip for multiplexed proteomic sample preparation and analysis by MALDI-MS," Lab Chip, vol. 6, no. 9, pp. 1213–1219, 2006.
- [13] S. P. Zhang et al., "Digital acoustofluidics enables contactless and programmable liquid handling," *Nature Commun.*, vol. 9, no. 1, 2018, Art. no. 2928.
- [14] Z. Li et al., "High-level synthesis for micro-electrode-dot-array digital microfluidic biochips," in Proc. Design Automation Conf., 2016, pp. 1–6.
- [15] W.-C. Chung et al., "Module placement under completion time uncertainty in micro-electrode-dot-array digital microfluidic biochips," *IEEE Trans. Multi-Scale Comput. Syst.*, vol. 4, no. 4, pp. 811–821, 2018.
- [16] O. Keszocze et al., "Exact routing for micro-electrode-dot-array digital microfluidic biochips," in Proc. Asia and South Pacific Des. Autom. Conf., 2017, pp. 708–713.
- [17] C. Jaress et al., "Rapid online fault recovery for cyber-physical digital microfluidic biochips," in Proc. IEEE VLSI Test Symp., 2015, pp. 1–6.
- [18] S. Windh et al., "Performance improvements and congestion reduction for routing-based synthesis for digital microfluidic biochips," *IEEE Trans. Comput. - Aided Des. Integr. Circuits Syst.*, vol. 36, no. 1, pp. 41–54, 2017.
- [19] Q. Wang et al., "Control-fluidic codesign for paper-based digital microfluidic biochips," in Proc. IEEE/ACM Int. Conf. Comput.-Aided Des., 2016, pp. 1–8.
- [20] P. Zhang et al., "Contactless, programmable acoustofluidic manipulation of objects on water," Lab Chip, vol. 19, no. 20, pp. 3397–3404, 2019.
- [21] "Basic fluidic operations," 2020. [Online]. Available: https://youtu.be/ 3EK5bvxrQx8
- [22] P. Zhang et al., "Acoustohydrodynamic tweezers via spatial arrangement of streaming vortices," Sci. Adv., to appear in 2020.
- [23] H. Bruus, Theoretical Microfluidics. Oxford: Oxford University Press, 2008, vol. 18
- [24] S. W. Walker and B. Shapiro, "Modeling the fluid dynamics of electrowetting on dielectric (EWOD)," *J. Microelectromech. Syst.*, vol. 15, no. 4, pp. 986–1000, 2006.
- [25] C. Jin et al., "Design and simulation of high-throughput microfluidic droplet dispenser for lab-on-a-chip applications," in Proc. Europ. COM-SOL Conf., 2014.
- [26] V. Bahadur et al., "An energy-based model for electrowetting-induced droplet actuation," J. Micromech. Microeng., vol. 16, no. 8, p. 1494, 2006.
- [27] MATLAB version 9.3.0.713579 (R2017b), The Mathworks, Inc., Natick, Massachusetts, 2017.
- [28] "MATLAB code for the model," 2020. [Online]. Available: https://drive.google.com/open?id=1F9DyZ7d-PzOWO-dE4iX3feQVW7fOYjQs
- [29] Z. Zhong et al., "Structural test and functional test for digital acoustofluidic biochips," in Proc. IEEE Int. Test Conf. (ITC), 2019, pp. 1–10.

- [30] D. Foresti et al., "Acoustophoretic contactless transport and handling of matter in air," Proc. Nat. Acad. Sci., vol. 110, no. 31, pp. 12 549–12 554, 2013.
- [31] "Droplet writing," 2020. [Online]. Available: https://youtu.be/ hwOsamKTk8s
- [32] "A simple bioassay," 2020. [Online]. Available: https://youtu.be/ 5IsyUGEr280
- [33] M. Elfar et al., "Synthesis of error-recovery protocols for micro-electrode-dot-array digital microfluidic biochips," ACM Trans. Embedded Comput. Syst., vol. 16, no. 5s, pp. 127-1–127-22, 2017.
- [34] P. R. Gascoyne and J. V. Vykoukal, "Dielectrophoresis-based sample handling in general-purpose programmable diagnostic instruments," *Proc. IEEE*, vol. 92, no. 1, pp. 22–42, 2004.
- [35] W. Zeng et al., "Finding shortest paths on real road networks: The case for A\*," Int. J. Geogr. Inf. Sci., vol. 23, no. 4, pp. 531–543, 2009.



Zhanwei Zhong received the bachelor's degree in electronic science and technology from Sun Yat-sen University, Guangzhou, China, in 2013, the master's degree in electronic engineering from Tsinghua University, Beijing, China, in 2016, and the Ph.D. degree in computer engineering from Duke University, Durham, USA, in 2020. He is currently a Senior DFT engineer with Marvell Semiconductor Inc. in Santa Clara, CA, USA. He was a DFT intern with AMD Inc. (Beijing) in 2017 and with Apple Inc. (Cupertino) in 2019. His research interests include

design automation for biochips, IJTAG test standard and design verification methodologies.



Haodong Zhu received the bachelor's degree in integrated science from Peking University, Beijing, China, in 2018. He is currently a Ph.D. Student in the Department of Mechanical Engineering and Materials Science at Duke University, Durham, NC, USA. His current research interests include digital acoustofluidics and acoustic streaming-based particle manipulation.



Peiran Zhang received the bachelor's degree in biochemistry and molecular biology from Ocean University of China, Qingdao, China, in 2014. He is currently a Ph.D. Student in the Department of Mechanical Engineering and Materials Science at Duke University, Durham, NC, USA. He is focusing on developing acoustic microfluidic techniques to enable lab automation for nanoscale to mesoscale samples in biomedical engineering.



James Morizio (Member, IEEE) received the B.S.E.E. degree from Virginia Polytechnic Institute, in 1982, and the M.S.E.E. degree from Univeristy of Colorado, in 1984. In 1995 he completed his Ph.D. degree in Electrical Engineering from Duke University under the direction of Dr. Jeff Derby. He has over 20 years corporate experience working with IBM Corporation and Mitsubishi Electronics America in the Research Triangle Park (RTP) in North Carolina, USA. He is currently a Research Assistant Professor of Electrical and Computer Engineering and is also

President of Triangle BioSystems, Inc., where he project leads numerous mixed-signal broadband and audio VLSI design projects. He conducts research in the areas of mixed-signal VLSI design and sub-system hardware development for biomedical instrumentation products. His current research is focussed on the design and test of telemetric, low power, integrated data acquisition systems for brain source neuron signals.



Tony Jun Huang (Fellow, IEEE) received the bachelor's degree and master's degree from Xi'an Jiaotong University, in 1996 and 1999, respectively, and the Ph.D. degree in mechanical and aerospace engineering from the University of California, Los Angeles (UCLA), in 2005. He is now the William Bevan Distinguished Professor at Department of Mechanical Engineering and Materials Science (MEMS) at Duke University. Previously he was a professor and the Huck Distinguished Chair in Bioengineering Science and Mechanics at Pennsylvania State University.

sity. His research interests are in the fields of acoustofluidics, optofluidics, and micro/nano systems for biomedical diagnostics and therapeutics. He has authored/co-authored over 230 peer-reviewed journal publications and 26 issued or pending patents in these fields. He was elected a fellow of the following six professional societies: the American Association for the Advancement of Science (AAAS), the American Institute for Medical and Biological Engineering (AIMBE), the American Society of Mechanical Engineers (ASME), the Institute of Electrical and Electronics Engineers (IEEE), the Institute of Physics (IoP), and the Royal Society of Chemistry (RSC). Huang's research has gained international recognition through numerous prestigious awards and honors including a 2010 National Institutes of Health (NIH) Director's New Innovator Award, a 2012 Outstanding Young Manufacturing Engineer Award from the Society for Manufacturing Engineering, a 2013 American Asthma Foundation (AAF) Scholar Award, JALA Top Ten Breakthroughs of the Year Award in 2011, 2013, and 2016, the 2014 IEEE Sensors Council Technical Achievement Award from the Institute of Electrical and Electronics Engineers (IEEE), the 2017 Analytical Chemistry Young Innovator Award from the American Chemical Society (ACS), the 2019 Van Mow Medal from the American Society of Mechanical Engineers (ASME), and the 2019 Technical Achievement Award from the IEEE Engineering in Medicine and Biology Society (EMBS).



Krishnendu Chakrabarty (Fellow, IEEE) received the B.Tech. degree from the Indian Institute of Technology, Kharagpur, in 1990, and the M.S.E. and Ph.D. degrees from the University of Michigan, Ann Arbor, in 1992 and 1995, respectively. He is now the John Cocke Distinguished Professor and Department Chair of Electrical and Computer Engineering and Professor of Computer Science at Duke University. Prof. Chakrabarty is a recipient of the National Science Foundation CAREER award, the Office of Naval Research Young Investigator award, the Humboldt

Research Award from the Alexander von Humboldt Foundation, Germany, the IEEE Transactions on CAD Donald O. Pederson Best Paper Award (2015), the ACM Transactions on Design Automation of Electronic Systems Best Paper Award (2017), and over a dozen best paper awards at major conferences. He is also a recipient of the IEEE Computer Society Technical Achievement Award (2015), the IEEE Circuits and Systems Society Charles A. Desoer Technical Achievement Award (2017), the IEEE Test Technology Technical Council Bob Madge Innovation Award (2018), and the Distinguished Alumnus Award from the Indian Institute of Technology, Kharagpur (2014). He is a Research Ambassador of the University of Bremen (Germany). He was a Hans Fischer Senior Fellow at the Institute for Advanced Study, Technical University of Munich, Germany, during 2016-2019. Prof. Chakrabarty's current research projects include: design-for-testability of integrated circuits and systems (especially 3D integration and system-on-chip); microfluidic biochips; hardware security; neuromorphic computing systems. He is a Fellow of ACM, a Fellow of AAAS, and a Golden Core Member of the IEEE Computer Society. He received the 2018 Invitational Fellowship of the Japan Society for the Promotion of Science (JSPS) in the Short Term S ("Nobel Prize level") category. He is a recipient of the 2008 Duke University Graduate School Deans Award for excellence in mentoring, and the 2010 Capers and Marion McDonald Award for Excellence in Mentoring and Advising, Pratt School of Engineering, Duke University. He has served as a Distinguished Visitor of the IEEE Computer Society (2005-2007, 2010-2012), a Distinguished Lecturer of the IEEE Circuits and Systems Society (2006-2007, 2012-2013), and an ACM Distinguished Speaker (2008-2016). Prof. Chakrabarty served as the Editor-in-Chief of IEEE Design & Test of Computers during 2010-2012, ACM Journal on Emerging Technologies in Computing Systems during 2010-2015 and IEEE Transactions on VLSI Systems during 2015-2018.